Express Polymer Letters Vol.17, No.1 (2023) 40–53
Available online at www.expresspolymlett.com
https://doi.org/10.3144/expresspolymlett.2023.4

Research article

Synthesis and properties of a novel waterborne photosensitive resin for 3D printing

Qinghong Luo[1], *Ting Zhang*[2], *Ruijie Xu*[1], *Hongping Xiang*[1], *Yanyan Cui*[1], *Zhiquan Li*[1], *Xiaoxuan Liu*[1*]

[1]School of Materials and Energy, Guangdong University of Technology, Guangzhou, 510006 Guangdong, PR China
[2]Chemistry & Environment Engineering, Shaoguan University, Shaoguan, 512005 Guangdong, PR China

Received 29 April 2022; accepted in revised form 22 August 2022

Abstract. A series of novel waterborne photosensitive resins were prepared successfully with poly(propylene oxide) bis(2-aminopropyl ether), tricyclodecane dimethanol diacrylate, 2-isocyanatoethyl acrylate, and hydrochloric acid by Michael addition reaction. The results show that with the increasing double bonds content, the double bonds conversion increases from 78.7, 85.6 to 92.8% in the photopolymerization, respectively, and the gel content of the UV-cured film increases from 48.05, 69.10 to 83.28%. In addition, the glass transition temperature and tensile strength of the UV-cured film follow the same increasing trend. Moreover, the content of hydrochloride has a great influence on the hydrophilicity of the waterborne photosensitive resins. The studies indicated that as the hydrochloride content decreases, the surface water contact angle of the UV-cured film increases from 10.8, 22.9 to 51.5°, and water absorption decreases from 26.55, 16.20 to 11.06%, respectively. Moreover, the waterborne photosensitive resins exhibited a high printing accuracy together with a good effect of washing and are promising for 3D printing.

Keywords: *mechanical properties, waterborne photosensitive resin, Michael addition reaction, photopolymerization, 3D printing application*

1. Introduction

3D printing (also known as 'additive manufacturing') is a manufacturing technology that transforms computer-aided and designed virtual models into 3D tangible objects through layer-by-layer deposition [1, 2]. It has the characteristics of creating unique structures, reducing material wastes, and increasing efficiency [3] and is widely used in the fields of biomedicine [4, 5], aerospace [6], education [7], and dentistry [8]. The 3D printing technology can be divided into several categories such as jetting, binder jetting, vat photopolymerization, energy deposition, powder bed fusion, material extrusion, and sheet lamination [9], where the more popular printing technology is vat photopolymerization [10] due to its incredibly high resolution and excellent surface finish for creating concept models, rapid prototyping and building complex geometries.

Vat photopolymerization 3D Printing, utilizing radiation to selectively polymerize liquid photosensitive resin in a vat to form a solid 3D structure [11], includes several printing processes [12]. Stereolithography (SLA) was developed as the first vat photopolymerization method in the early 1980s [13]. Since then, various new vat photopolymerization methods have been developed, including digital projection lithography (DLP) [14], continuous liquid interface production (CLIP) [15], and computed axial lithography (CAL) [16], to meet the speed and resolution demands of printing.

In vat photopolymerization 3D printing, the model is first designed by CAD software and converted into

---

[*] Corresponding author, e-mail: p-xxliu@gdut.edu.cn

a standard (STL) format file. Then the STL format model is sliced and printed according to the different requirements of the printing equipment. After printed, the model is removed from the platform, rinsed with organic solvents such as isopropyl alcohol (IPA) to remove the liquid resin layer from the surface of 3D printed parts, and post-cured under UV light to improve the mechanical properties [10]. The removal of support structures, rinsing, and post-curing steps are required processes for almost all 3D printing systems [17]. Without these steps, harmful monomers may remain on or inside the item, and there is an increased risk of conformational distortion [18].

In the post-processing of vat photopolymerization 3D printing, almost all printed parts need to be rinsed with organic solvents. Invernizzi [19], He *et al*. [20], and Silbert *et al*. [21] used ethanol to remove residual resin from the surface of printed parts; Peterson *et al*. [22], Mubarak *et al*. [23], and Garcia *et al*. [24] reported isopropanol as a cleaning agent for the post-processing of 3D printing; Schmidt *et al*. [25] also used phenoxyethanol for the post-processing. However, the use of organic solvents increases the risk of fire and can pollute the environment. Using waterborne photosensitive resin can eliminate safety risks associated with organic solvents for the surface cleaning of printed parts. Therefore, developing a waterborne photosensitive resin suitable for 3D printing is of great interest.

In this paper, a series of waterborne photosensitive resins were designed and synthesized via the Michael addition reaction between amino and acrylate double bond. After evaluating the mechanical properties, the waterborne photosensitive resin was applied to 3D printing, and the printing accuracy and washability of the printed objects were evaluated.

2. Experimental

2.1. Materials

Poly(propylene oxide) bis(2-aminopropyl ether) (D400): M_n = 400 g/mol, Huntsman Polyurethane (China) Co., Ltd., Shanghai, China. 2-isocyanatoethyl acrylate (AOI) was purchased from Shanghai Cabchem New Materials Technology Co., Ltd., Shanghai, China. Tricyclodecane dimethanol diacrylate (TCDDA) was supplied by Eternal Materials Co., Ltd., Zhuhai, China. 2-hydroxyethyl methacrylate (HEMA), tetrahydrofuran (THF), and anhydrous magnesium sulfate were purchased from Macklin, Shanghai, China. Hydrochloric acid was purchased from Guangdong Guangshi Reagent Technology Co., Ltd., Guangzhou, China. Photoinitiator: ethyl(2,4,6-trimethylbenzoyl) phenylphosphinate (L-TPO) was provided by Tianjin Jiuri New Material Co., Ltd., Tianjin, China. Acryloyl-morpholine (ACMO) was supplied by Beijing RBL Chemicals Co., Ltd., Beijing, China. All of the reagents were used as received without further purification.

2.2. Synthesis of the asymmetrical monomer

A four-necked flask, equipped with a mechanical stirrer, condenser, thermometer, and constant funnel, was charged with HEMA (14.75 g, 0.11 mol) and cooled using a water bath while stirring, then AOI (14.11 g, 0.1 mol) was slowly added to the flask with a constant pressure funnel at 30~35 °C. The mixture was reacted at 40~42 °C for 4 h under stirring to obtain the asymmetrical monomer. The reaction continued until the absorption peak of the –NCO group in the infrared spectrum disappeared. Finally, after being washed 3 times with deionized water and dried over anhydrous $MgSO_4$, a transparent, colorless liquid has been obtained, namely the asymmetrical monomer (H-AOI) [26, 27]. The specific reaction route is shown in Figure 1a.

2.3. Synthesis of the waterborne photosensitive resin

The waterborne photosensitive resin (WPR) was prepared with TCDDA, D400, H-AOI, AOI, and hydrochloric acid by polyaddition reactions. The specific reaction route is shown in Figure 1b. The details of preparation were as follows [28, 29]. TCDDA and D400 were added into a flask and heated to 40 °C under stirring. After the absorption peak of the –C=C group (1640 cm^{-1}) in the infrared spectrum disappeared, H-AOI was added to the flask. The mixtures were maintained at 42 °C until the absorption peak of the $–NH_2$ group (1590 cm^{-1}) in the infrared spectrum disappeared completely to afford an oligomer capped with an acrylate double bond. Then, AOI was added via a dropping funnel with the temperature at 40~42 °C, keeping the temperature until the absorption peak of the –NCO group (2267 cm^{-1}) vanished. Finally, WPR was obtained after hydrochloric acid was slowly added to neutralize the secondary amino group under stirring. The waterborne photosensitive resins were named WPR-1, WPR-2, and WPR-3, respectively, according to the different amounts of the

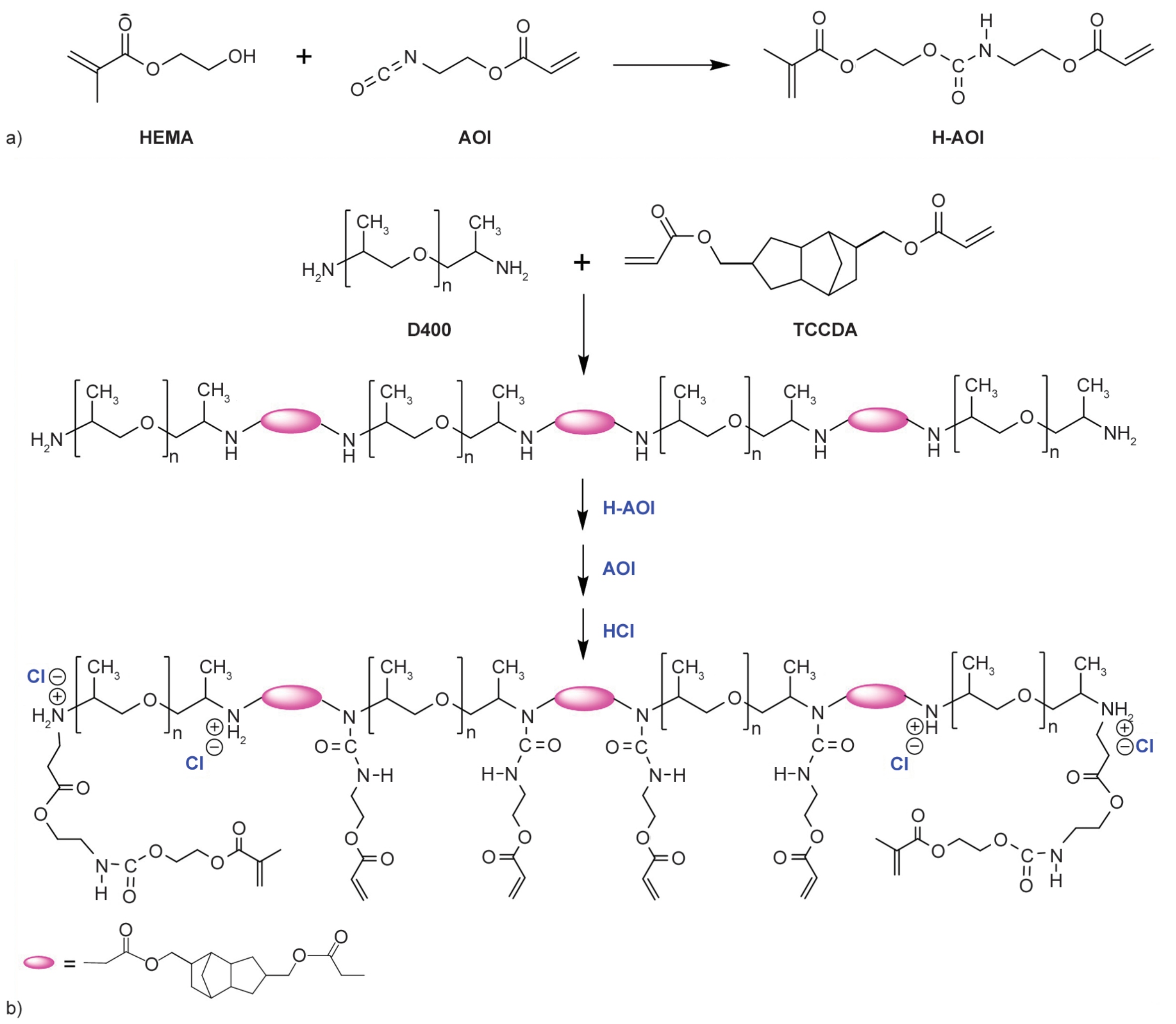

Figure 1. Synthetic routes of a) H-AOI and b) waterborne photosensitive resin.

–C=C group. The ratio of each component is illustrated in Table 1.

2.4. Fabrication of the UV-cured film

First, WPR was mixed with L-TPO at a ratio of 97.0 to 3.0 to produce the acrylic composition. Second, the WPR UV-cured films were prepared by pouring the acrylic composition on a cleaned polytetrafluoroethylene mold (50 mm × 15 mm × 2 mm) and dried at room temperature under dark conditions for 12 h to form a liquid layer. Subsequently, the liquid layer was irradiated under a UV curing machine (model: RX300-1; power lamp: 2000 W; the distance of the lamp: 10 cm, Dongguan Ergu Optoelectronics Technology Co. Ltd., Dongguan, China) for 10 s to afford the UV-cured film after dried at 50 °C under a vacuum for 12 h, the films were peeling off from the Teflon mold for a follow-up test.

3. Methods

3.1. Characterization

Fourier transform infrared (FTIR) spectra were obtained on Nicolet 560 infrared spectrometer (Thermo Fisher Scientific, Germany) using a disc of KBr in

Table 1. Synthetic composition of waterborne photosensitive resins.

Materials Samples	D400 [g]	DCPDA [g]	H-AOI [g]	AOI [g]	HCl[1] [g]	DBC[2] [mmol/g]	SC[3] [%]
WPR-1	40.00	22.83	13.56	7.06	14.72	1.02	90.58
WPR-2	40.00	22.83	13.56	14.12	9.81	1.50	93.86
WPR-3	40.00	22.83	13.56	21.18	4.91	1.95	96.99

[1] The concentration of hydrochloric acid is 37.2%.
[2] DBC is an abbreviation for double bond content, calculated according to the formula [30]
[3] SC is an abbreviation for solid content.

the range of 4000~600 $\mathrm{cm^{-1}}$ with 4 $\mathrm{cm^{-1}}$ resolution over 32 scans at room temperature.

The proton nuclear magnetic resonance (^{1}H NMR) spectra of the samples were recorded at 25 °C by Bruker AVANCE III HD 400 spectrometer (Bruker, Switzerland) with deuterated chloroform as the solvent.

The loss factor curves, storage modulus, and loss modulus at different temperatures was measured with a TA Instruments DMA 50 (Metravib co., Ltd., France) in tensile mode at 1 Hz and 10 µm amplitude with a heating rate of 3 °C/min and temperature scan from –20 to 80 °C. The samples were cut into squareness with approximate dimensions of 10 mm × 5 mm × 2 mm.

The tensile properties of the UV-cured film of WPR were evaluated using a SANS CMT 6000 Universal Tester (MTS Systems Co., Ltd., America) in accordance with GB/T 528-2009 at room temperature. Dumbbell-shaped specimens (length: 50 mm, thickness: 2 mm, the width of parallel part: 4 mm, according to GB/T 1040.2–2010) were made for the tensile tests, and a deformation speed of 50 mm/min was employed in the test process. Each measurement was repeated at least three times, and the results were averaged.

Thermal degradation behavior of the UV-cured film of WPR was assessed by thermogravimetric analysis with Mettler TGA/SDTA 851 thermogravimetric analyzer (TGA) (Mettler, Switzerland) in 20 ml/min N_2 atmosphere from 30 to 600 °C with a heating rate of 10 °C/min, sample weight about 5.0~10.0 mg.

Contact angle measurements were conducted on a static drop contact angle measuring instrument (JC2000C1, Shanghai Zhongchen Digital Technic Apparatus Co., Ltd., China). The samples were fixed on a movable stage horizontally with a size of 3.0 cm × 3.0 cm, and the water droplets were deposited on the surface of the samples by a micro-syringe. A CCD video camera was used to record the shape of the droplet and an image analyzing software to determine the contact angle evolution. The experimental results were the average values of five measurements performed for each sample.

The conversion of acrylate double bonds

The conversion of acrylate double bond during UV irradiation was determined by real-time infrared spectra on a Nicolet iS50 FTIR at room temperature. The liquid waterborne photosensitive resins were coated on KBr disc with a thickness of approximately 100 µm and then irradiated *in situ* by an M-Ultra violet light source (MUA-165, Mejiro Genossen, Japan) with a dominant wavelength of 365 nm. Each spectrum obtained from the IR spectrometer was an average of 4 scans with a resolution of 8 $\mathrm{cm^{-1}}$. The peak area variation of –C=C– stretching vibration of acrylate double bond at 1640 $\mathrm{cm^{-1}}$ was used to determine their conversion (γ) according to Equation (1) [31]:

$$\gamma = \frac{A_0 - A_t}{A_0} \cdot 100\% \tag{1}$$

where A_0 and A_t were the normalized peak area of acrylate double bonds before and after UV radiation at time t, respectively.

The gel content, which reflected the crosslinking degree of the UV-cured film of WPR, was measured with the Soxhlet extraction method. After drying for 12 h at 40 °C under vacuum, the WPR films and THF were added into the Soxhlet extractor and heated to reflux for 24 h . Afterward, the remaining WPR films were dried at 40 °C for 12 h. We compared the residual mass with the initial mass to obtain the gel content value by Equation (2) [32]:

$$G = \frac{w_t}{w_0} \cdot 100\% \tag{2}$$

where G means gel content, w_0 represents initial mass, and w_t represents final mass.

The weighing method assessed the water absorption behaviors of the UV-cured film of WPR. The WPR cured films were cut into specimens with dimensions 10 mm × 10 mm × 1 mm and dried at 50 °C for 12 h to obtain the weight of samples (m_0). Then the samples were immersed in deionized water for 24 h. Hereafter, the samples were taken out to remove the surface moisture, and the weight of samples (m_t) was obtained. The water absorption rate (W) of the samples was calculated according to Equation (3), [33]:

$$W = \frac{m_t - m_0}{m_0} \cdot 100\% \tag{3}$$

3.2. 3D printing

The diluted monomer ACMO and L-TPO were added to WPR after evenly mixed and left to stand in the dark for defoaming before use. The 3D printing was performed on an Iron Box/CH-10 3D Printer

(Shenzhen Shengma Youchuang Technology Co., Ltd., Shenzhen, China) with $\lambda_{max} \sim 405$ nm and layer height of 0.05 mm, bottom layer exposure time of 60 s, bottom layer count of 6 and layer exposure time of 15 s (irradiation intensity: 1.0 mW/cm^2, lifting speed 65 mm/min, return speed 150 mm/min).

Curing depth measurement

A 405 nm LED light was employed as the light source (Model: UVEC-4 II,Tianjin Lamplik Lighting Electric Co. Ltd., Tianjin, China). A spot area with a 10 mm diameter was exposed in the center of the transparent plastic container filled with waterborne photosensitive resin. The cured disks were taken out and cleaned with paper towels. The thickness of the disks was measured with an IP54 micrometer gauge (Dongguan Orient Precision Measurement Technology Co., Ltd., Dongguan, China). The light intensity was kept at 10.3 mW/cm^2 for all experiments and the exposure time was 2~10 s. Each exposure was done in triplicate, and the mean values were calculated.

Determination of photosensitive parameters

The light absorption of photosensitive resin follows the Beer-Lambert law [34]. The penetration depth (*Dp*), cure depth (*Cd*), exposure (E [mJ/cm^2]), and the critical exposure (E_C) Equation (4):

Table 2. The waterborne photosensitive resin composition of 3D printing.

Samples Materials	*S1* [g]	*S2* [g]	*S3* [g]	*S4* [g]
WPR-2	85.0	75.0	60.0	55.0
ACMO	15.0	25.0	40.0	45.0
L-TPO	0.3	0.3	0.3	0.3

$$Cd = Dp\ln\left[\frac{E}{E_C}\right] \tag{4}$$

where *Dp* is the penetration depth of the waterborne photosensitive resin, denoting the UV absorption intensity of the waterborne photosensitive resin; E is the actual exposure intensity of the waterborne photosensitive resin. E_C is the critical exposure.

By transforming Equation (4), a general linear equation is formed, as Equation (5):

$$Cd = Dp\ln E - Dp\ln E_C \tag{5}$$

where *Dp* and *Dp*,lnE_C are the constants, *i.e.* the slope and intercept of the corresponding linear fitting curve, respectively. By comparing Equation (5), the value of *Dp* and E_C can be deduced.

4. Results and discussion

4.1. Structure analysis of H-AOI

The FTIR spectra of AOI and H-AOI are shown in Figure 2a. The absorption peak of N–H stretching vibration appears at 3368 cm^{-1}, the absorption peak of N–H bending vibration is 1533 cm^{-1} [35], and the absorption peak at 1730 cm^{-1} belongs to the stretching vibration of the carbonyl group (C=O). This is the characteristic peak of the carbamate group, resulting from the reaction of isocyanate groups (–NCO) with hydroxyl groups (–OH). In addition, the characteristic peak at 2267 cm^{-1} attributed to the isocyanate group (–NCO) disappeared completely. The results of FTIR spectra clearly confirm the successful reaction between HEMA and AOI.

The ^{1}H NMR spectrum of H-AOI is shown in Figure 2b. The peaks at 6.10~6.45 ppm are contributed by the proton of methacrylate double bond

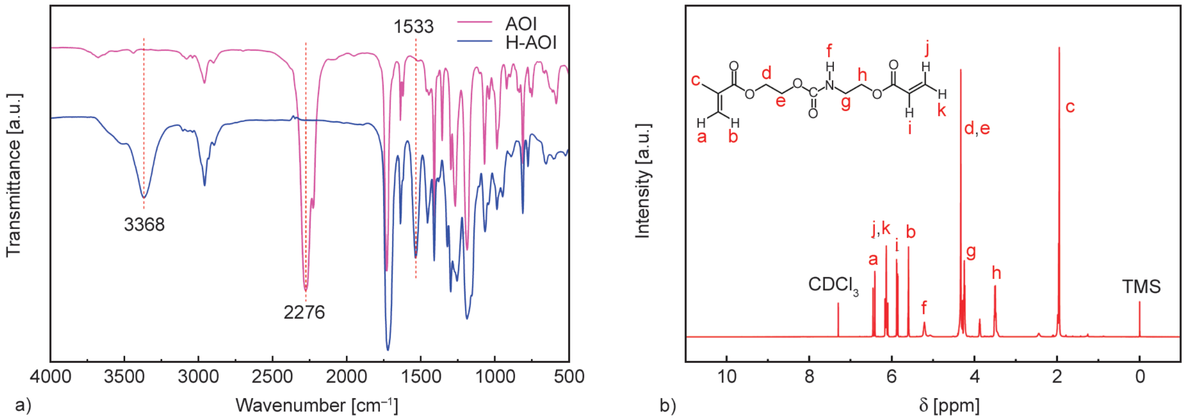

Figure 2. a) FTIR spectra af AOI and H-AOI, b) ^{1}H NMR spectrum of asymmetric monomer (H-AOI).

(CH_2–$C(CH_3)$–). The peaks at 6.09~6.16, 5.50~5.60 ppm are ascribed to the proton of acrylate double bond (–CH–CH_2). The peaks at 4.21~4.33 and 3.47~3.5 ppm are attributed to the proton of methylene (–CH_2–) [36]. The peaks at 1.95 ppm correspond to the protons of methyl (–CH_3). The peaks at 5.21 ppm are attributed to the protons of the carbamate (–NHCOO–). The results of ^{1}H NMR indicate that H-AOI was successfully prepared.

4.2. Structure analysis of WPR

D400, TCDDA, and H-AOI are used to prepare prepolymers containing methacrylic double bonds by Michael addition reaction, and then the secondary amine groups react with isocyanate groups of AOI to insert different proportions of acrylate double bonds in the side chain of the prepolymer. Finally, hydrochloric acid is used to form a salt with the residual secondary amine groups to impart hydrophilicity to the prepolymer. The FTIR spectra of the reactants, intermediate prepolymers, and products are shown in Figure 3. Figure 3a curve (1) is the FTIR spectrum of TCDDA. The characteristic absorption peaks of the carbon-carbon double bond at 1640 and 810 cm^{-1} could be clearly observed. After the reaction, the peaks disappear completely, as shown in Figure 3a curve (2), indicating the double bonds of TCDDA are consumed when reacting with D400 by Michael addition and forming an amino-terminated prepolymer (denoted as PR-1). Figure 3a curve (3) is the FTIR spectrum of the product of PR-1 reacting with H-AOI. The characteristic absorption peaks of carbon-carbon double bonds at 1640, 810 cm^{-1} and the carbamate at 3320, 1533 cm^{-1} are observed, demonstrating that H-AOI is reintroduced successfully and forming the prepolymer with acrylate moieties (denoted as PR-2). Figure 3a curve (4) is the FTIR spectrum of PR-2 reacting with AOI. The characteristic absorption peaks of the isocyanate group at 2267 cm^{-1} disappear, indicating AOI reacts with the secondary amine groups of PR-2, producing the prepolymer (denoted as PR-3). The FTIR spectrum of WPR is shown in Figure 3a curve (5). The characteristic absorption peak of hydrochloride at 2459 cm^{-1} appears, indicating hydrochloride formed from hydrogen chloride reacting with the secondary amino group of prepolymer PR-3.

Figure 3b is the ^{1}H NMR spectrum of WPR. The peaks 5.60~6.45, and 4.51~4.66 ppm are contributed by the proton of carbon-carbon double bond and carbamate, respectively. The results of ^{1}H NMR combined with FTIR confirmed WPR was successfully synthesized.

4.3. Photopolymerization kinetics of waterborne photosensitive resin

Real-time FTIR is robust means of monitoring polymerization *in situ*. The characteristic absorption peaks of the acrylate double bond at 1640 and 810 cm^{-1}are shown in Figure 4a as a function of irradiation time. As can be seen, the absorption intensity of characteristic peaks gradually decreased with increasing irradiation time, indicating that the double bonds were consumed during the polymerization.

Figure 4b shows the double bond conversion curves of WPR-1, WPR-2, and WPR-3. As shown in Figure 4b, the double bond conversions of WPR-1, WPR-2, and WPR-3 gradually increase up to 78.7, 85.6, and 92.8%, respectively. Under UV irradiation, the photoinitiator is cracked into free radicals. With

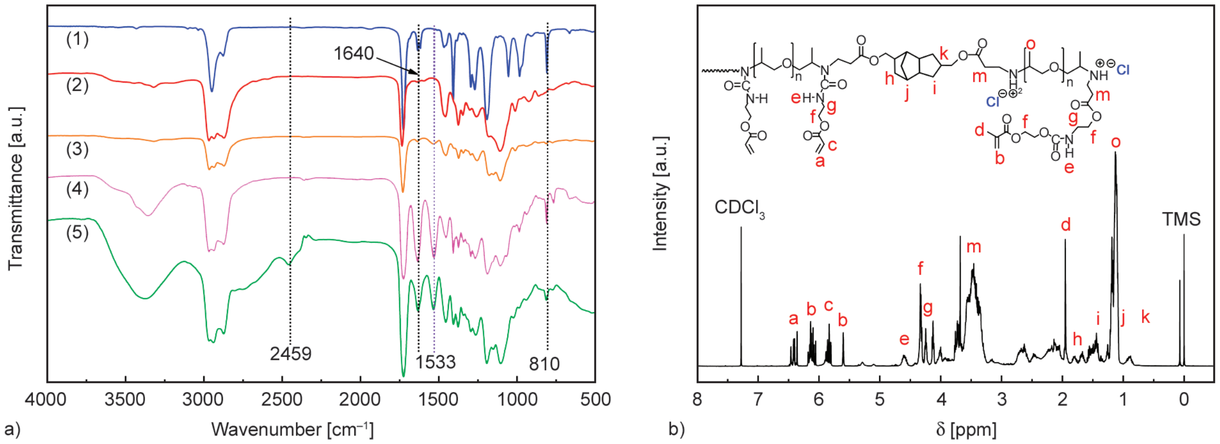

Figure 3. a) (1)–(5) are the FTIR spectra of TCDDA, PR-1, PR-2, PR-3, and WPR, respectively, b) is the ^{1}H NMR spectrum of WPR.

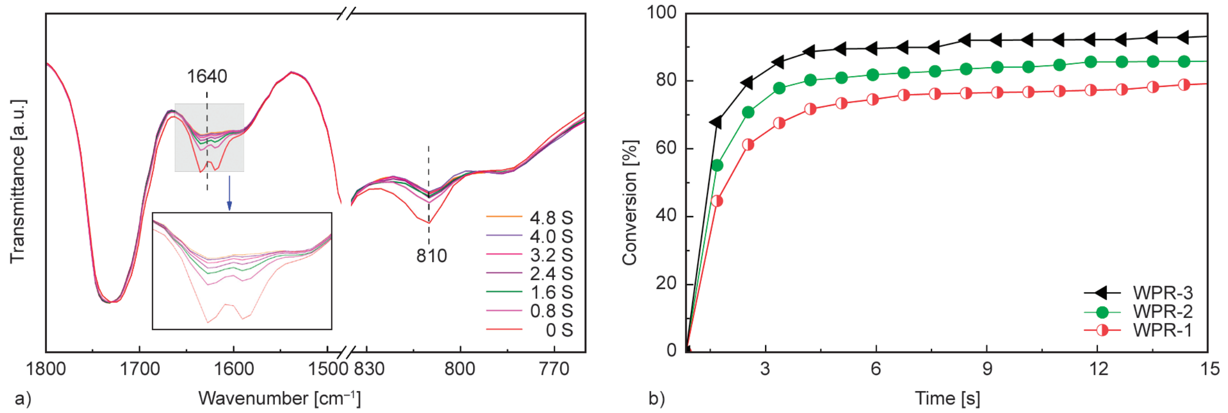

Figure 4. a) The absorption intensity *vs*. irradiation time for the double bonds. b) The double bonds conversion of WPR under UV irradiation with the intensity of 50 mJ/cm^2 and the L-TPO concentrations of 1.0 wt%.

the increasing double bond content, the probability of free radicals attacking the double bonds increases. Therefore, the number of active radicals produced by chain reaction increases, and the polymerization rate and double bond conversion of WPR increase with the increase of the double bond content.

4.4. Tensile strength

The stress-strain curves, change trend of tensile strength, and gel content of the UV-cured films of WPR is shown in Figure 5. As shown in Figure 5a, the tensile strength gradually increases from 0.35, 1.40 to 2.58 MPa, while the elongation at break decreases from 44.0, 40.9 to 40.3% for WPR-1, WPR-2, and WPR-3, respectively. This is mainly because the crosslinking density of WPR cured films increases with the increasing acrylate double bond content, leading to the formation of fixable macromolecular chains and a rigid crosslinking network. Figure 5b shows that the gel contents of WPR-1, WPR-2, and WPR-3 gradually increase from 48.05 and 69.10 to 83.28%, respectively. The tensile strength of the UV-cured films increases with increasing gel contents, demonstrating that the gel contents have a great effect on the tensile strength of the UV-cured films of WPR.

4.5. Dynamic mechanical analysis

Dynamic mechanical analysis (DMA) was conducted to measure the glass transition temperature, which is an important performance parameter of polymeric materials. Figure 6 shows the storage modulus (E') and loss factor ($\tan\delta$) of the UV-cured films of WPR as a function of temperature, respectively. As Figure 6a shows, the storage modulus E' of the UV-cured films of WPR increase for WPR-1, WPR-2, and WPR-3. In addition, the double bond content of WPR-1, WPR-2, and WPR-3 are correspondingly 1.02, 1.50, and 1.95 (Table 1). Obviously, the storage modulus E' of the UV-cured films of WPR increase with the increasing double bond content of WPR resins. This is mainly because the increasing double

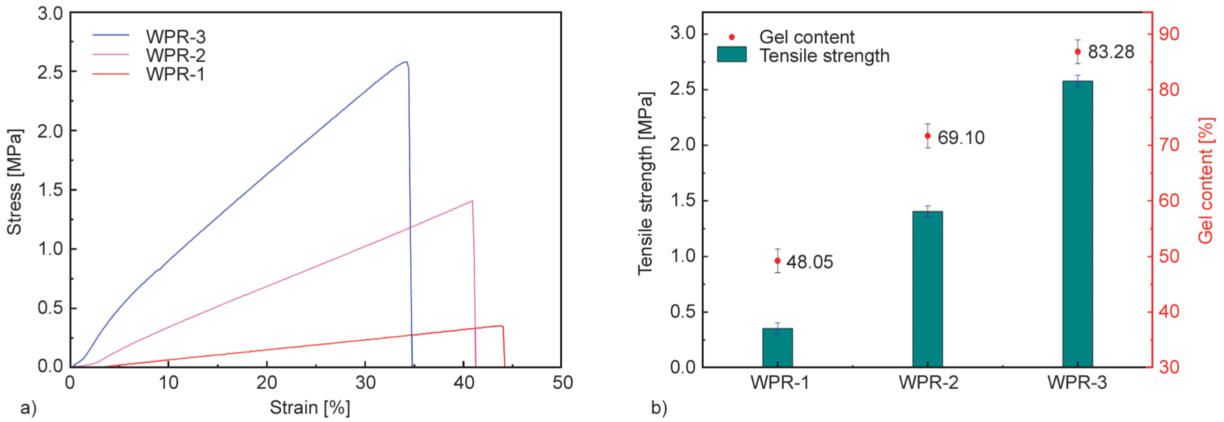

Figure 5. a) The stress-strain curves of the UV-cured films. b) The changing trend of tensile strength and gel contents of the UV-cured films.

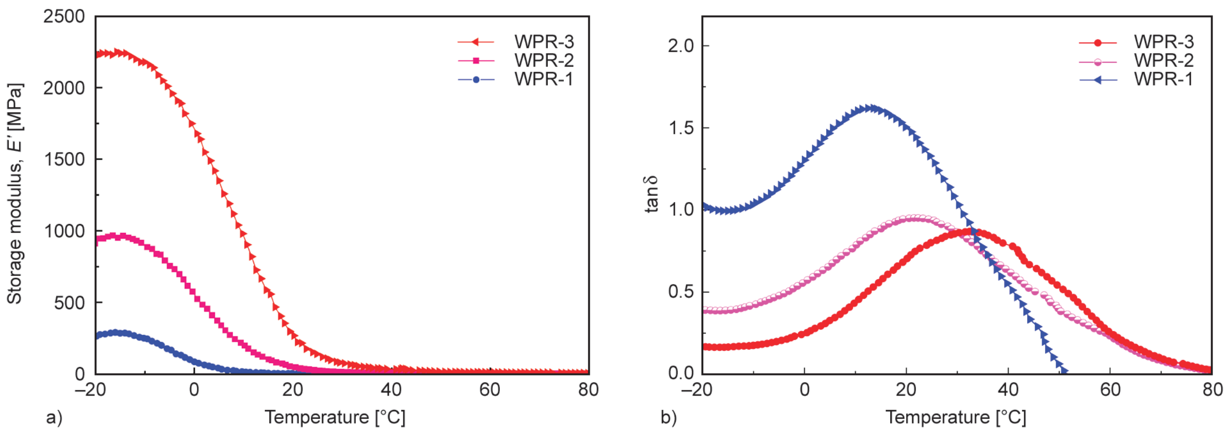

Figure 6. a) The storage modulus of the UV-cured films of WPR as a function of temperature. b) Tan δ of the UV-cured films of WPR as a function of temperature.

bond content of WPR leads to the increased crosslinking degree of the UV-cured films of WPR, which results in the storage modulus *E*′ increasing.

The glass transition temperature of the UV-cured films of WPR was evaluated by the maximum of tan δ curve [37]. As shown in Figure 6b and Table 1, with the increasing acrylate double bond content of WPR, the glass transition of the UV-cured films of WPR increases from 13.5 and 21.5 to 32.4 °C, respectively. The enhancement can be explained by the increase of double bond content, improving the crosslinking degree of the UV-cured film, causing restriction of the molecular chain movement.

4.6. Water absorption of WPR cured film

Figure 7a shows the water contact angle, and water absorption of WPR cured films. The surface water contact angle of the UV-cured films of WPR-1, WPR-2, and WPR-3 gradually increases with the values of 10.8, 22.9 and 51.5°, respectively. It is caused by the decreasing content of the hydrophilic groups in the corresponding WPR-1, WPR-2, and WPR-3 resin, which reduces the surface energy of the UV-cured film and leads to an increase in the surface water contact angle. Furthermore, the crosslinking density is an important factor affecting the water contact angle of the UV-cured film. The crosslinking density of the UV-cured films increases with the increasing double bond content of the WPR resin, which leads to the surface water contact angle arising.

In addition, with the increase in water contact angle, the water absorption of the UV-cured films of WPR-1, WPR-2, and WPR-3 gradually decreased, which were 26.6, 16.2, and 11.1%, respectively. This is mainly due to the decrease of hydrophilicity of the UV-cured films with the decrease of hydrophilic group content, *i.e.*, the increase of hydrophobicity, which leads to the increase of difficulty for water molecules to enter the cured films. Furthermore, the increase in the content of acrylate double bonds in WPR-1, WPR-2, and WPR-3 also leads to an increase in the crosslinking density after UV irradiation, which reduces the water absorption of the UV-cured films. Therefore, the content of the hydrophilic group and the crosslinking density are important factors affecting the water absorption and contact angle of cured films.

In WPR resins, the hydrophilic group is hydrochloride, which has good water solubility. The increasing

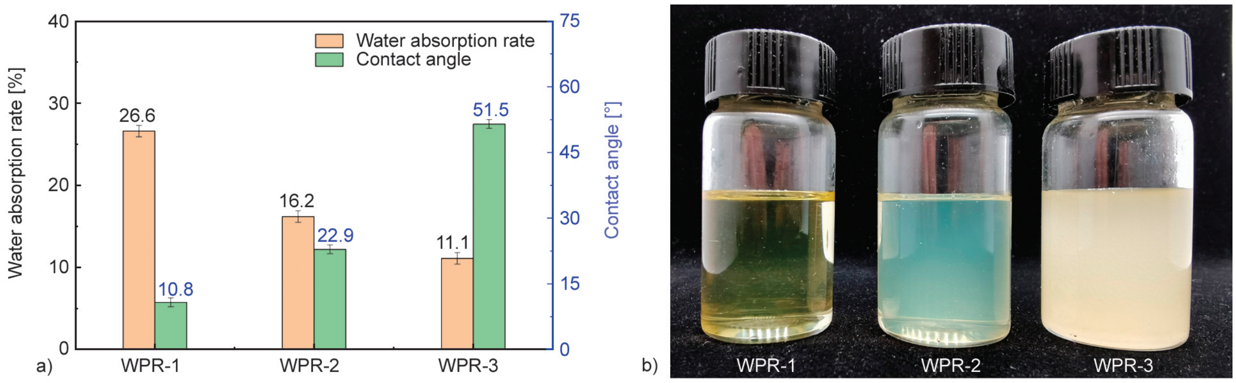

Figure 7. a) Surface water contact angle and water absorption of the UV-cured film. b) The water solubility of WPR.

content of hydrochloride could improve the hydrophilicity of WPR. Figure 7b shows the appearance of the WPR resins after the addition of 40% water. By comparing the appearance of the solutions of WPR-1, WPR-2, and WPR-3, it can be seen that WPR-1 is pale yellow and transparent, WPR-2 is light blue and transparent, and WPR-3 is cloudy. This is mainly because a decrease in the content of hydrochloride resulted in the decrease in hydrophilicity of WPR-1, WPR-2, and WPR-3. Overall, WPR resins have good water solubility and good water-washing properties.

4.7. Thermal stability of the WPR cured film

The thermal stability of WPR cured film was measured by the TG-DTG. Figure 8a shows the thermogravimetric (TG) curves of the UV-cured films of WPR-1, WPR-2, and WPR-3. It can be seen from the curves that the mass gradually decreases as the temperature increases. The temperatures are listed in Table 3. A weight loss of 5%, denoted as $T_{5\%}$, is usually considered to be the initial decomposition temperature of the materials. As shown in Table 3, the initial decomposition temperatures of the UV-cured films of WPR-1, WPR-2, and WPR-3 were 111.5, 128.3, and 218.3 °C, respectively. That is mainly due to the residual moisture in the UV-cured films of WPR-1 and WPR-2, resulting in the initial decomposition temperature occurring at a low-temperature stage. The decomposition temperature $T_{10\%}$ of the UV-cured films of WPR-1, WPR-2, and WPR-3 increased from 212.0 and 235.0 to 260.5 °C. This is mainly because an increase in crosslinking density of the UV-cured films resulted from the acrylate double bond content of WPR arising.

Figure 8b shows the differential thermogravimetric (DTG) curves of the UV-cured films of WPR-1, WPR-2, and WPR-3. The thermal decomposition process of WPR cured films is divided into four main stages. The maximum decomposition rates for each stage are listed in Table 3. The first stage occurs before 180 °C, which is mainly due to the residual water in the cured film. The second stage occurs between 230 and 255 °C, with a mass loss of approximately 10%. The main reason for the second stage is the decomposition of hydrochloride due to the dissociation of ionic bonds. The third stage occurs between 310 and 350 °C with a mass loss of 40~48%, mainly due to the decomposition of ether bonds and carbamates. The fourth stage occurs between 380 and 450 °C and is mainly caused by the decomposition of carbon-carbon bonds. Further comparison of the three curves shows that the mass loss rate decreases with increasing temperature in the order of WPR-1, WPR-2, and WPR-3, which is mainly due to the increase in crosslinking density of the cured films.

Table 3. Thermal stability of the UV-cured film of WPR.

Samples	$T_{5\%}$ [°C]	$T_{10\%}$ [°C]	First step		Second step		Third step		Fourth step	
			T_{max} [°C]	Weight loss [%]	T_{max} [°C]	Weight loss [%]	T_{max} [°C]	Weight loss [%]	T_{max} [°C]	Weight loss [%]
WPR-1	111.5	212.0	98.2	3.9	230.8	12.2	316.3	48.2	385.2	84.9
WPR-2	128.3	235.0	98.7	2.7	244.5	11.3	327.7	41.1	392.5	77.0
WPR-3	218.3	260.5	107.3	1.7	253.3	8.9	346.5	40.1	390.3	68.2

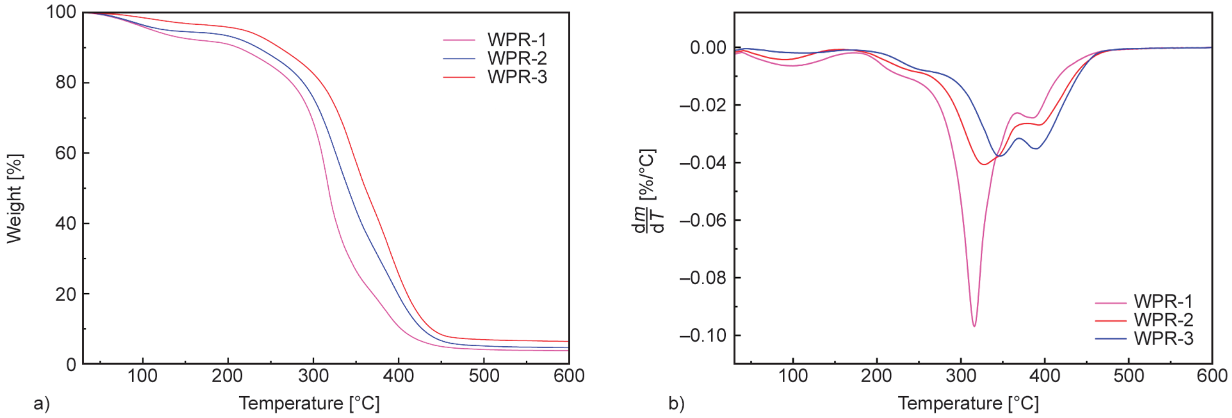

Figure 8. Thermal stability of the UV-cured film of WPR, a) TGA, and b) DTG curves.

4.8. 3D printing

UV-curing 3D printing, with the characteristics of high printing accuracy and fast printing speed, is a kind of additive manufacturing technology. In traditional UV-curing 3D printing, the photosensitive resins are oil-soluble, and a large amount of organic solvent is required to clean the surface of the printed parts. The use of organic solvents increases the risk of fire and could cause environmental pollution problems. The issues could be addressed effectively by the use of waterborne photosensitive resins for 3D printing because the residual resin of printed parts surface could be cleaned by water. The prepared WPR-2 resin was evenly mixed with diluted monomer ACMO and the photoinitiator L-TPO in certain proportions for 3D printing tests. The specific proportions are shown in Table 2.

The viscosity of waterborne photosensitive resins has a significant impact on 3D printing. The viscosity of the resin is adjusted by adding ACMO for the convenience of 3D printing. The added ACMO has a great effect on the mechanical properties of 3D printed parts. The favorable ratio for 3D printing was determined by comparing the tensile strength of 3D printed parts and the viscosity of the resin. As shown in Figure 9, the tensile strength of 3D printed parts increases with the amount of added ACMO rising. Formulation *S1* and *S2* are unsuitable for 3D printing due to their high viscosity. Formulation *S4* and *S3* with lower viscosities can be used for 3D printing. In addition, the tensile strength and the amount of ACMO added are relatively higher.

Determination of waterborne photosensitive parameters

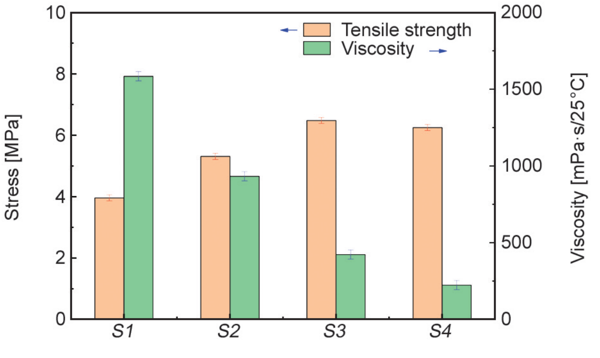

Figure 9. The viscosity of 3D printing composition and the tensile strength of the printed parts.

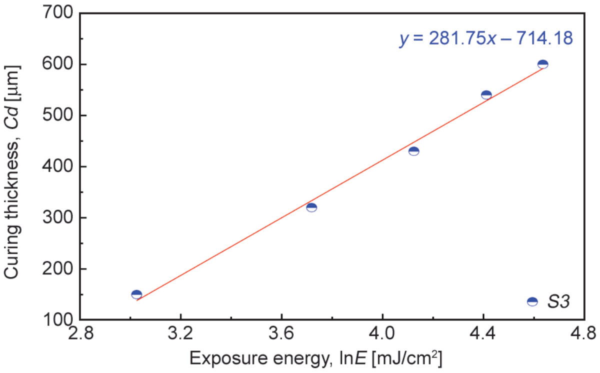

Figure 10. Curves fitted and extrapolated to determine the photosensitive parameters of *S3* with 40.0 wt% ACMO and 3.0 wt% photoinitiator (L-TPO).

The penetration depth (*Dp*) and critical exposure (E_C) are important parameters to adjust the exposure time in a 3D printer to cure the chosen layer thickness. All 3D printing photosensitive resins can be described with the parameters of *Dp* and E_C [38]. The exposure intensity *E* is a function of the exposure time multiplied with the incident light intensity of the LED light source. The penetration depth (*Dp*) and critical exposure (E_C) can be plotted in a linear form (10.3 mW/cm^2 for the LED light source used in this study). Thus, *E* is a function of exposure time (the range of 2~10 s), and *Cd* can be directly measured for each experiment. Hence, the critical exposure energy (E_C) and the penetration depth (*Dp*) can be plotted in a linear form, based on the known values of *E* and *Cd*. As shown in Figure 10, it is a linear fitting curve of critical exposure energy (E_C) and penetration depth (*Dp*) for formulation *S3*. It shows a very good fit to the data of the measured value *E* and *Cd*. The bottom-up 3D printing vat polymerization technology is a layer-by-layer additive manufacturing process. Therefore, it is necessary the value of actual cure depth is larger than the sliced layer thickness of the printed sample to ensure sufficient adhesion between the layers [34]. In addition, the exposure energy *E* must be larger than the critical exposure intensity E_C to initiate polymerization reaction. It can be achieved by adjusting the exposure time. From Figure 10, the value of penetration depth (Dp = 281.75 μm) and critical exposure (E_C = 12.61 mJ/cm^2) of the formulation S3 can be obtained by calculation. In 3D printing, the printing accuracy of photosensitive resin is an important parameter. In this paper, a hollow cube model is designed to test the printing accuracy. The printed hollow cube is shown in Figure 11a. The hollow cube model was designed by CAD, and the ridge length of a single hollow cube is 10 times the ridge width. The entire hollow cube was fabricated via 3D printing with dimensions of

15 mm × 15 mm × 15 mm (Figure 11d). The ridge width of the printed hollow cube can be calculated (205.5 µm). The 3D printed part of the hollow cube model has a high printing accuracy (the strip width

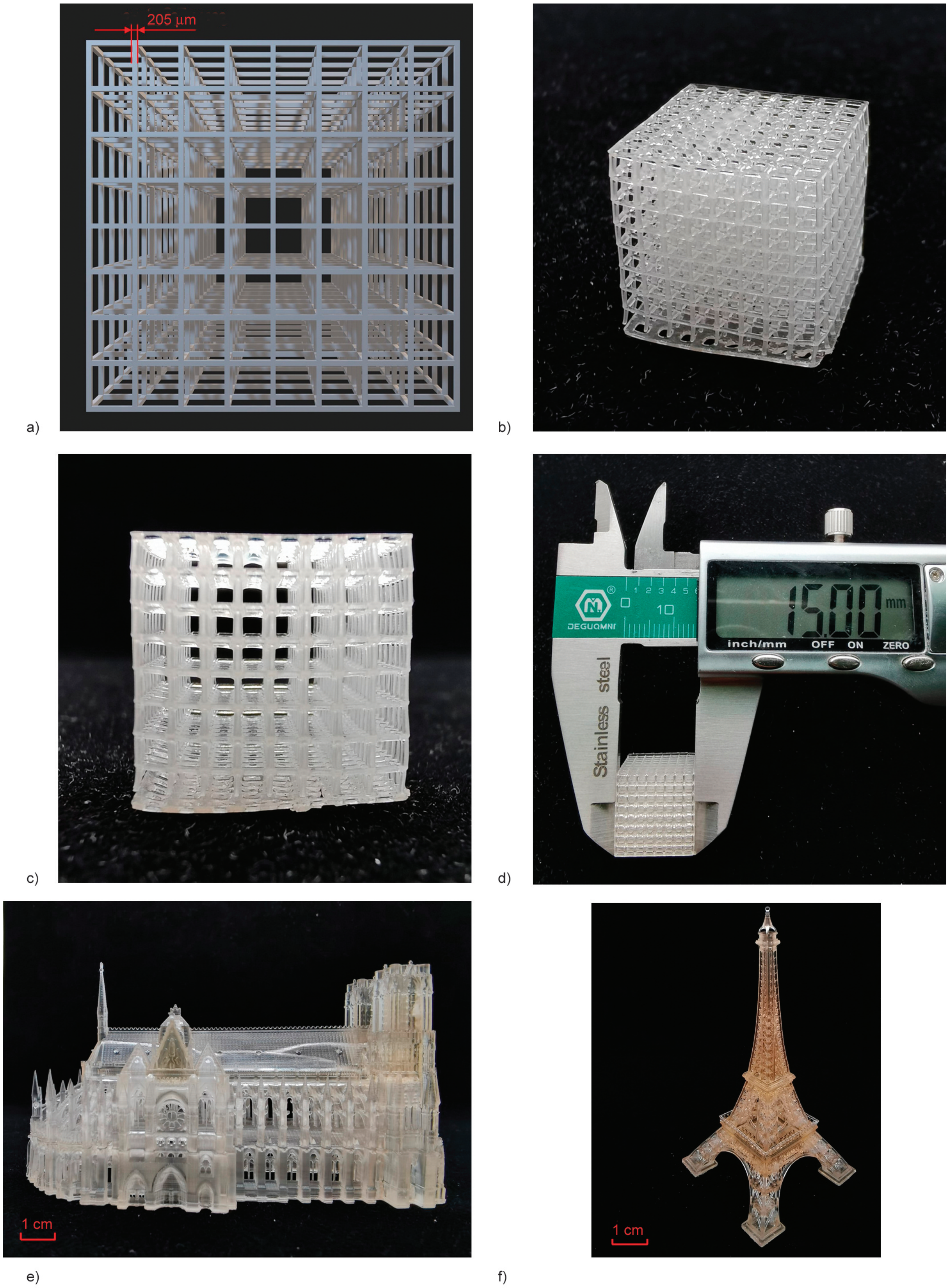

Figure 11. a) The 3D model of hollow cube design by CAD. b) Hollow cube printed using formulation S3; c) Front view of printed hollow cube. d) The size of a hollow cube. e), f) The printed model of Reims Cathedral and Eiffel tower was printed using formulation *S3*.

is about 205 μm). The printed hollow cube with different view aspects is shown in Figures 11b and 11c, which has a good printing effect.

As shown in Figure 11e and Figure 11f, two building models with a highly complex structure was successfully fabricated, indicating that the prepared waterborne photosensitive resin could be promising for dentistry and jewelry manufacturing.

5. Conclusions

An asymmetrical monomer and a series of novel waterborne photosensitive resins were successfully synthesized and confirmed by FTIR and ^{1}H NMR spectroscopy. The effects of different double bonds content were investigated and found that with increasing double bonds content, the double bonds conversion increases from 78.7, 85.6 to 92.8% in photopolymerization of WPR, and the gel content of the cured film increases from 48.05, 69.10 to 83.28%, the glass transition temperature and tensile strength of WPR cured film follow the same increasing trend. Moreover, the content of hydrochloride has a great influence on the hydrophilicity of the waterborne photosensitive resin. The studies indicated that as the hydrochloride content decreases, the surface water contact angle of the UV-cured film of WPR increases from 10.8, 22.9 to 51.5°, and water absorption decreases from 26.55, 16.20, to 11.06%. Finally, waterborne photosensitive resins were applied to 3D printing, and the photosensitive parameters, including the penetration depth (Dp = 281.64 μm) and critical exposure (E_C = 12.78 mJ/cm^2) were measured. Above all, the waterborne photosensitive resins exhibited a high printing accuracy and good effect of washing and are promising for waterborne 3D printing.

Acknowledgements

The authors thank the support from the Key R&D Program of Guangdong Province (Grant No. 2020B090924001), the National Natural Science Foundation of China (Grants: 51873043) and the JieYang Sailing Program (Grants: CXTD2021001).

References

[1] Li J., Pumera M.: 3D printing of functional microrobots. Chemical Society Reviews, **50**, 2794–2838 (2021). https://doi.org/10.1039/d0cs01062f

[2] Frazier W. E.: Metal additive manufacturing: A review. Journal of Materials Engineering and Performance, **23**, 1917–1928 (2014). https://doi.org/10.1007/s11665-014-0958-z

[3] Ngo T. D., Kashani A., Imbalzano G., Nguyen K. T. Q., Hui D.: Additive manufacturing (3D printing): A review of materials, methods, applications and challenges. Composites Part B: Engineering, **143**, 172–196 (2018). https://doi.org/10.1016/j.compositesb.2018.02.012

[4] Chia H. N., Wu B. M.: Recent advances in 3D printing of biomaterials. Journal of Biological Engineering, **9**, 4 (2015). https://doi.org/10.1186/s13036-015-0001-4

[5] Seoane-Viaño I., Januskaite P., Alvarez-Lorenzo C., Basit A. W., Goyanes A.: Semi-solid extrusion 3D printing in drug delivery and biomedicine: Personalised solutions for healthcare challenges. Journal of Controlled Release, **332**, 367–389 (2021). https://doi.org/10.1016/j.jconrel.2021.02.027

[6] Joshi S. C., Sheikh A. A.: 3D printing in aerospace and its long-term sustainability. Virtual and Physical Prototyping, **10**, 175–185 (2015). https://doi.org/10.1080/17452759.2015.1111519

[7] McMenamin P. G., Quayle M. R., McHenry C. R., Adams J. W.: The production of anatomical teaching resources using three-dimensional (3D) printing technology. Anatomical Sciences Education, **7**, 479–486 (2014). https://doi.org/10.1002/ase.1475

[8] Dawood A., Marti B. M., Sauret-Jackson V., Darwood A.: 3D printing in dentistry. British Dental Journal, **219**, 521–529 (2015). https://doi.org/10.1038/sj.bdj.2015.914

[9] Alghamdi S. S., John S., Choudhury N. R., Dutta N. K.: Additive manufacturing of polymer materials: Progress, promise and challenges. Polymers, **13**, 753 (2021). https://doi.org/10.3390/polym13050753

[10] Pagac M., Hajnys J., Ma Q-P., Jancar L., Jansa J., Stefek P., Mesicek J.: A review of vat photopolymerization technology: Materials, applications, challenges, and future trends of 3D printing. Polymers, **13**, 598 (2021). https://doi.org/10.3390/polym13040598

[11] Tan L. J., Zhu W., Zhou K.: Recent progress on polymer materials for additive manufacturing. Advanced Functional Materials, **30**, 2003062 (2020). https://doi.org/10.1002/adfm.202003062

[12] Bagheri A., Jin J.: Photopolymerization in 3D printing. ACS Applied Polymer Materials, **1**, 593–611 (2019). https://doi.org/10.1021/acsapm.8b00165

[13] Kodama H.: Automatic method for fabricating a three-dimensional plastic model with photo-hardening polymer. Review of Scientific Instruments, **52**, 1770–1773 (1981). https://doi.org/10.1063/1.1136492

[14] Lu Y., Mapili G., Suhali G., Chen S., Roy K.: A digital micro-mirror device-based system for the microfabrication of complex, spatially patterned tissue engineering scaffolds. Journal of Biomedical Materials Research: Part A, **77**, 396–405 (2006). https://doi.org/10.1002/jbm.a.30601

[15] Tumbleston J. R., Shirvanyants D., Ermoshkin N., Janusziewicz R., Johnson A. R., Kelly D., Chen K., Pinschmidt R., Rolland J. P., Ermoshkin A., Samulski E. T., DeSimone J. M.: Continuous liquid interface production of 3D objects. Science, **347**, 1349–1352 (2015). https://doi.org/10.1126/science.aaa2397

[16] Kelly B. E., Bhattacharya I., Heidari H., Shusteff M., Spadaccini C. M., Taylor H. K.: Volumetric additive manufacturing *via* tomographic reconstruction. Science, **363**, 1075–1079 (2019). https://doi.org/10.1126/science.aau7114

[17] Karakurt I., Lin L.: 3D printing technologies: Techniques, materials, and post-processing. Current Opinion in Chemical Engineering, 28**,** 134–143 (2020). https://doi.org/10.1016/j.coche.2020.04.001

[18] Elbadawi M., McCoubrey L. E., Gavins F. K. H., Ong J. J., Goyanes A., Gaisford S., Basit A. W.: Harnessing artificial intelligence for the next generation of 3D printed medicines. Advanced Drug Delivery Reviews, **175**, 113805 (2021). https://doi.org/10.1016/j.addr.2021.05.015

[19] Invernizzi M., Suriano R., Muscatello A., Turri S., Levi M.: Near-visible stereolithography of a low shrinkage cationic/free-radical photopolymer blend and its nanocomposite. Journal of Applied Polymer Science, **137**, 48333 (2020). https://doi.org/10.1002/app.48333

[20] He C., Ma C., Li X., Yan L., Hou F., Liu J., Guo A.: Polymer-derived SiOC ceramic lattice with thick struts prepared by digital light processing. Additive Manufacturing, **35**, 101366 (2020). https://doi.org/10.1016/j.addma.2020.101366

[21] Silbert S. D., Simpson P., Setien R., Holthaus M., La Scala J., Ulven C. A., Webster D. C.: Exploration of biobased functionalized sucrose ester resins for additive manufacturing *via* stereolithography. ACS Applied Polymer Materials, **2**, 2910–2918 (2020). https://doi.org/10.1021/acsapm.0c00417

[22] Peterson G. I., Schwartz J. J., Zhang D., Weiss B. M., Ganter M. A., Storti D. W., Boydston A. J.: Production of materials with spatially-controlled cross-link density via vat photopolymerization. ACS Applied Materials and Interfaces, **8**, 29037–29043 (2016). https://doi.org/10.1021/acsami.6b09768

[23] Mubarak S., Dhamodharan D., Divakaran N., Kale M. B., Senthil T., Wu L., Wang J.: Enhanced mechanical and thermal properties of stereolithography 3D printed structures by the effects of incorporated controllably annealed anatase TiO_2 nanoparticles. Nanomaterials, **79**, 79 (2020). https://doi.org/10.3390/nano10010079

[24] Garcia E. A., Ayranci C., Qureshi A. J.: Material property-manufacturing process optimization for form 2 VAT-photo polymerization 3D printers. Journal of Manufacturing and Materials Processing, **4**, 12 (2020). https://doi.org/10.3390/jmmp4010012

[25] Schmidt J., Altun A. A., Schwentenwein M., Colombo P.: Complex mullite structures fabricated via digital light processing of a preceramic polysiloxane with active alumina fillers. Journal of the European Ceramic Society, **39**, 1336–1343 (2019). https://doi.org/10.1016/j.jeurceramsoc.2018.11.038

[26] Sugimoto H., Tonouchi S., Toda K., Nakanishi E.: Preparation and mechanical properties of acryl/glass cloth composite materials with low light dispersion. Journal of Polymer Research, **27**, 39 (2020). https://doi.org/10.1007/s10965-019-1998-8

[27] Yang Z., Peng H., Wang W., Liu T.: Crystallization behavior of poly(ε-caprolactone)/layered double hydroxide nanocomposites. Journal of Applied Polymer Science, **116**, 2658–2667 (2010). https://doi.org/10.1002/app.31787

[28] Hong C-Y., You Y-Z., Wu D-C., Liu Y., Pan C-Y.: Thermal control over the topology of cleavable polymers: From linear to hyperbranched structures. Journal of the American Chemical Society, **129**, 5354–5355 (2007). https://doi.org/10.1021/ja070871+

[29] Moszner N., Völkel T., Rheinberger V.: Synthesis, characterization and polymerization of dendrimers with methacrylic end groups. Macromolecular Chemistry and Physics, **197**, 621–631 (1996). https://doi.org/10.1002/macp.1996.021970217

[30] Bai C. Y., Zhang X. Y., Dai J. B., Li W. H.: A new UV curable waterborne polyurethane: Effect of C=C content on the film properties. Progress in Organic Coatings, **55**, 291–295 (2006). https://doi.org/10.1016/j.porgcoat.2005.12.002

[31] Xiang H., Wang X., Ou Z., Lin G., Yin J., Liu Z., Zhang L., Liu X.: UV-curable, 3D printable and biocompatible silicone elastomers. Progress in Organic Coatings, **137**, 105372 (2019). https://doi.org/10.1016/j.porgcoat.2019.105372

[32] Dong X., Ren J., Duan Y., Wu D., Lin L., Shi J., Jia R., Xu X., He X.: Preparation and properties of green UV-curable itaconic acid cross-linked modified waterborne polyurethane coating. Journal of Applied Polymer Science, **139**, 52042 (2022). https://doi.org/10.1002/app.52042

[33] Wang J., Zhang H., Miao Y., Qiao L., Wang X., Wang F.: UV-curable waterborne polyurethane from CO_2-polyol with high hydrolysis resistance. Polymer, **100**, 219–226 (2016). https://doi.org/10.1016/j.polymer.2016.08.039

[34] Hofstetter C., Orman S., Baudis S., Stampfl J.: Combining cure depth and cure degree, a new way to fully characterize novel photopolymers. Additive Manufacturing, **24**, 166–172 (2018). https://doi.org/10.1016/j.addma.2018.09.025

[35] Lin Z., Deng H., Hou Y., Liu X., Xu R., Xiang H., Peng Z., Rong M., Zhang M.: Dual-crosslinking side chains with an asymmetric chain structure: A facile pathway to a robust, self-healable, and re-dissolvable polysiloxane elastomer for recyclable flexible devices. Journal of Materials Chemistry A, **10**, 11019–11029 (2022). https://doi.org/10.1039/d2ta01535h

[36] Mori H., Miyamura Y., Endo T.: Synthesis and characterization of water-soluble silsesquioxane-based nanoparticles by hydrolytic condensation of triethoxysilane derived from 2-hydroxyethyl acrylate. Langmuir, **23**, 9014–9023 (2007). https://doi.org/10.1021/la700706a

[37] Pang Y., Shiraishi A., Keil D., Popov S., Strehmel V., Jiao H., Gutmann J. S., Zou Y., Strehmel B.: NIR-sensitized cationic and hybrid radical/cationic polymerization and crosslinking. Angewandte Chemie-International Edition, **60**, 1465–1473 (2021). https://doi.org/10.1002/anie.202010746

[38] Steyrer B., Busetti B., Harakály G., Liska R., Stampfl J.: Hot lithography vs. room temperature DLP 3D-printing of a dimethacrylate. Additive Manufacturing, **21**, 209–214 (2018). https://doi.org/10.1016/j.addma.2018.03.013